# Material assembly from collective action of shape-changing polymers

Mustafa K. Abdelrahman ®[1], Robert J. Wagner ®[2,3],
Manivannan Sivaperuman Kalairaj ®[4], Mason Zadan ®[5], Min Hee Kim[4],
Lindy K. Jang ®[4,6], Suitu Wang[1], Mahjabeen Javed[4], Asaf Dana ®[4],
Kanwar Abhay Singh ®[4], Sarah E. Hargett[4], Akhilesh K. Gaharwar ®[4],
Carmel Majidi ®[5], Franck J. Vernerey ®[2] & Taylor H. Ware ®[1,4] ✉

Some animals form transient, responsive and solid-like ensembles through dynamic structural interactions. These ensembles demonstrate emergent responses such as spontaneous self-assembly, which are difficult to achieve in synthetic soft matter. Here we use shape-morphing units comprising responsive polymers to create solids that self-assemble, modulate their volume and disassemble on demand. The ensemble is composed of a responsive hydrogel, liquid crystal elastomer or semicrystalline polymer ribbons that reversibly bend or twist. The dispersions of these ribbons mechanically interlock, inducing reversible aggregation. The aggregated liquid crystal elastomer ribbons have a 12-fold increase in the yield stress compared with cooled dispersion and contract by 34% on heating. Ribbon type, concentration and shape dictate the aggregation and govern the global mechanical properties of the solid that forms. Coating liquid crystal elastomer ribbons with a liquid metal begets photoresponsive and electrically conductive aggregates, whereas seeding cells on hydrogel ribbons enables self-assembling three-dimensional scaffolds, providing a versatile platform for the design of dynamic materials.

Materials capable of autonomous assembly, reconfiguration and disassembly in response to changes in environmental conditions may enable new functionality in robotics[1,2], medicine[3] and other engineering disciplines[4–7]. Inspiration for these materials can be found in animals that form transient structures through collective action to perform tasks not achievable by individual agents. Fire ants (*Solenopsis invicta*)[8], honeybees (*Apis mellifera*)[9] and California blackworms (*Lumbriculus variegatus*)[10] mechanically interlock into entangled swarms to accomplish various collective functions such as raft formation[11], colony unification[12] and thermal regulation[13]. Consequently, these animals form porous structures with viscoelastic mechanical properties[14] that exhibit adaptive self-assembly and reorganization due to each member's ability to physically attach and detach to its neighbours[12,15–17].

The key characteristics of these living aggregates, such as autonomous aggregation, solid-like viscoelasticity, internal motion, adaptability and reversible disassembly, are highly sought after in engineering materials[5]. Like their biological counterparts, synthetic aggregates can form free-standing structures with tunable mechanical properties[18–21]. For example, injectable hydrogel microspheres[22,23] that crosslink after injection form porous macroscopic solids; however, chemical crosslinking between units restricts disassembly. Colloidal systems, such as Janus particles[24] and microbubbles[25], demonstrate

[1]Department of Materials Science and Engineering, Texas A&M University, College Station, TX, USA. [2]Mechanical Engineering Department, Materials Science and Engineering Program, University of Colorado, Boulder, CO, USA. [3]Department of Mechanical and Aerospace Engineering, Cornell University, Ithaca, NY, USA. [4]Department of Biomedical Engineering, Texas A&M University, College Station, TX, USA. [5]Department of Mechanical Engineering, Carnegie Mellon University, Pittsburgh, PA, USA. [6]Materials Engineering Division, Lawrence Livermore National Laboratory, Livermore, CA, USA. ✉e-mail: Taylor.Ware@tamu.edu

reversible transitions from dispersed to clustered states under the influence of various stimuli[26–28]. These colloids generally exhibit a negligible cohesive strength. Improved cohesion is, however, achievable via mechanical entanglement. Entangled hydrogel microstrands[29] can form structures with sufficient cohesion to remain solid-like after moulding or three-dimensional (3D) printing. However, these aggregates are inactive and thus incapable of autonomous assembly, internal reconfiguration, adaptive response and disassembly.

We describe a general approach to create transient, responsive solids by exploiting the shape change of stimuli-responsive polymers[30–32]. Specifically, we employ hydrogel, elastomer and semicrystalline ribbons that undergo reversible, thermoresponsive transitions from straight to bent and/or twisted configurations on a change in environmental conditions[33–36]. This local transformation causes neighbouring ribbons to mechanically interlock and form solid-like ensembles with viscoelastic properties. Removing the stimulus causes the ribbons to straighten such that the aggregates redisperse into a disentangled suspension with negligible elasticity. We modulate the ribbon material type, shape and concentration to control the formation, mechanical properties and reversibility of aggregates. Ultimately, we demonstrate a largely material-agnostic strategy to assemble materials using shape-changing elements.

## Actuating ribbons form programmable, entangled aggregates

Liquid crystal elastomer (LCE) ribbons undergo a broad nematic–paranematic phase transition on heating, causing local contraction along the director[37] (Fig. 1a). We synthesize ribbons with controlled bending and twisting on heating due to a 90° rotation of the nematic director through the ribbon's thickness (Supplementary Fig. 1). By varying the relative angle $\theta$ of the ribbon's long axis to the orientation of the nematic director of the top surface, the relative degree of bending and twisting on actuation may be tuned, where $\theta = 0°$ induces pure bending, whereas $\theta = 45°$ induces pure twisting (Supplementary Fig. 2). When these ribbons are suspended in a fluid at sufficiently high concentrations and heated, ribbons mechanically interlock and contract to form solid-like ensembles, paralleling the activity-driven contraction of fire ant rafts (Fig. 1b)[8,14,38] or the $O_2$-concentration-modulated aggregation of California blackworms[13]. At high temperatures (150 °C), the aggregates have a greater storage modulus than loss modulus up to shear strains of 4.10 ± 0.43%, constituting a solid-like behaviour (Fig. 1c,d). On cooling, the LCE ribbons return to the nematic state, driving the ribbons towards their straight configurations, enabling redispersion into the liquid-like state. Specifically, when cooled to 50 °C, the system exhibits a greater loss than storage modulus from low strain amplitudes (>0.19 ± 0.04%) (Fig. 1d).

Thermoresponsive hydrogel and semicrystalline LCE ribbons can also be programmed to reversibly transition from a straight to bent configuration and therefore form transient aggregates in response to temperature (Supplementary Fig. 3). These responses occur over different temperature ranges, enabling aggregate formation at 25 °C (for semicrystalline LCEs), 37 °C (for hydrogels) and 175 °C (for LCEs). Furthermore, the elastic modulus of the constituents contributes to the mechanical properties of the aggregate. As the elastic modulus of the shape-changing material increases from 0.045 ± 0.002 MPa (hydrogels) to 22.160 ± 3.740 MPa (LCEs) and 382.170 ± 78.280 MPa (semicrystalline LCEs)[39], the yield stress of the aggregate increases from 2.35 ± 0.96 Pa (hydrogels) to 9.13 ± 4.90 Pa (LCEs) and 390.71 ± 78.24 Pa (semicrystalline LCEs) (Fig. 1e and Supplementary Figs. 4 and 5). After dispersion, the yield stress reduces to 0.32 ± 0.28 Pa for hydrogels, 0.16 ± 0.04 Pa for elastomers and 1.60 ± 0.19 Pa for semicrystalline LCEs (Fig. 1e).

Aggregates formed from the entanglement of ribbons exhibit unusual thermomechanical responses. Entanglement-induced solidification occurs on heating, analogous to the heat-induced solidification observed in some polymer solutions with a lower critical solution temperature[40]. These aggregates also exhibit large decreases in volume on heating (Supplementary Video 1). By contrast, bulk LCEs undergo nearly isochoric deformation by contracting along the nematic director and expanding perpendicularly. This volumetric contraction is driven by the underlying ribbons' decrease in end-to-end distance as they physically entangle and continue to twist during heating. Cooling allows the actuated ribbons to extend, lengthening the distance between physical entanglements and causing volumetric expansion. Materials that demonstrate volume contraction on heating are useful for applications where managing thermal stresses is required. However, the fabrication of such materials can be difficult as thermal expansion coefficients must be patterned within a single structure[41]. Here we achieve emergent volume contraction on heating within a self-assembled structure composed of a single material. The combination of a controlled phase transition and volumetric contraction enables LCE aggregates to structurally reform after damage without external manipulation (Supplementary Fig. 6). Furthermore, this combination enables LCE aggregates to form in confined environments such as fluidic channels (Supplementary Note 1 and Supplementary Figs. 7–9).

Aggregate formation is not ubiquitous amongst all ribbon suspensions. Rather, it depends on factors such as ribbon length and concentration. Short ribbons and suspensions with a low ribbon concentration fail to aggregate. Utilizing both experimentation and Monte Carlo simulations, we find that the initial suspensions of ribbons must exhibit percolated geometric overlap before actuation to form cohesive solids after heating (Supplementary Note 2 and Extended Data Fig. 1). However, once cohesive solids are formed, aggregates resist dilution, compression, shear and tension. Qualitative tensile (Supplementary Video 2) and dilution tests were conducted to explore the difference between the formed aggregates and solely jammed granular matter, which can be stiff in compression[42] yet cannot withstand tension or dilution[43]. To illustrate that these aggregates' structural stability goes beyond jamming, samples were transferred to a large, heated silicone oil bath with a rotating spin vane. Aggregates remain intact, indicating strong cohesion (Supplementary Video 3). In contrast, aggregates in cold, agitated silicone oil disperse.

## Aggregate properties are tunable through ribbon design

The aggregates' mechanical properties are highly influenced by the aspect ratios of the underlying ribbons. To map this dependence, we first conducted mechanical testing on aggregates formed from ribbons with conserved offset angles, cross-sectional areas and packing densities, as their lengths are swept over 3, 6 and 12 mm (Fig. 2a). We find that increasing the ribbon length increases the number of turns within each ribbon in the heated state (Supplementary Fig. 10). Longer ribbons form aggregates with higher yield strains, yield stresses and penetration forces (Fig. 2b–d and Supplementary Figs. 11 and 12). As the ribbon length is increased from 3 to 6 and 12 mm, the yield stress of the heated aggregate increases from 221 ± 61 Pa (at 2.10 ± 0.59% strain) to 300 ± 50 Pa (at 4.15 ± 0.43% strain) and 701 ± 114 Pa (at 6.98 ± 1.35% strain), respectively (Fig. 2b,c). After cooling without any other intervention, the yield stress decreases to 21 ± 17 Pa (at 0.06 ± 0.05% strain) for 3 mm ribbons, 25 ± 5 Pa (at 0.19 ± 0.04% strain) for 6 mm ribbons and 92 ± 28 Pa (at 0.27 ± 0.05% strain) for 12 mm ribbons (Fig. 2c and Supplementary Fig. 11). Furthermore, the formed aggregates resist probe penetration, having a normal force of 3.5 ± 1.0 N for 3 mm ribbons, 11.0 ± 1.0 N for 6 mm ribbons and 17.0 ± 2.0 N for 12 mm ribbons (Fig. 2d and Supplementary Fig. 12). Once cooled, the penetration force decreased to 0.03 ± 0.02 N for aggregates constructed from both 3 and 6 mm ribbons. However, the penetration force only decreased to 4.94 ± 0.90 N for the samples constructed from 12 mm ribbons. This indicates that there is a limit to the dissociation of aggregates, as discussed later. Since increasing a ribbon's length increases the number of twists it achieves on unfettered actuation, we hypothesize that
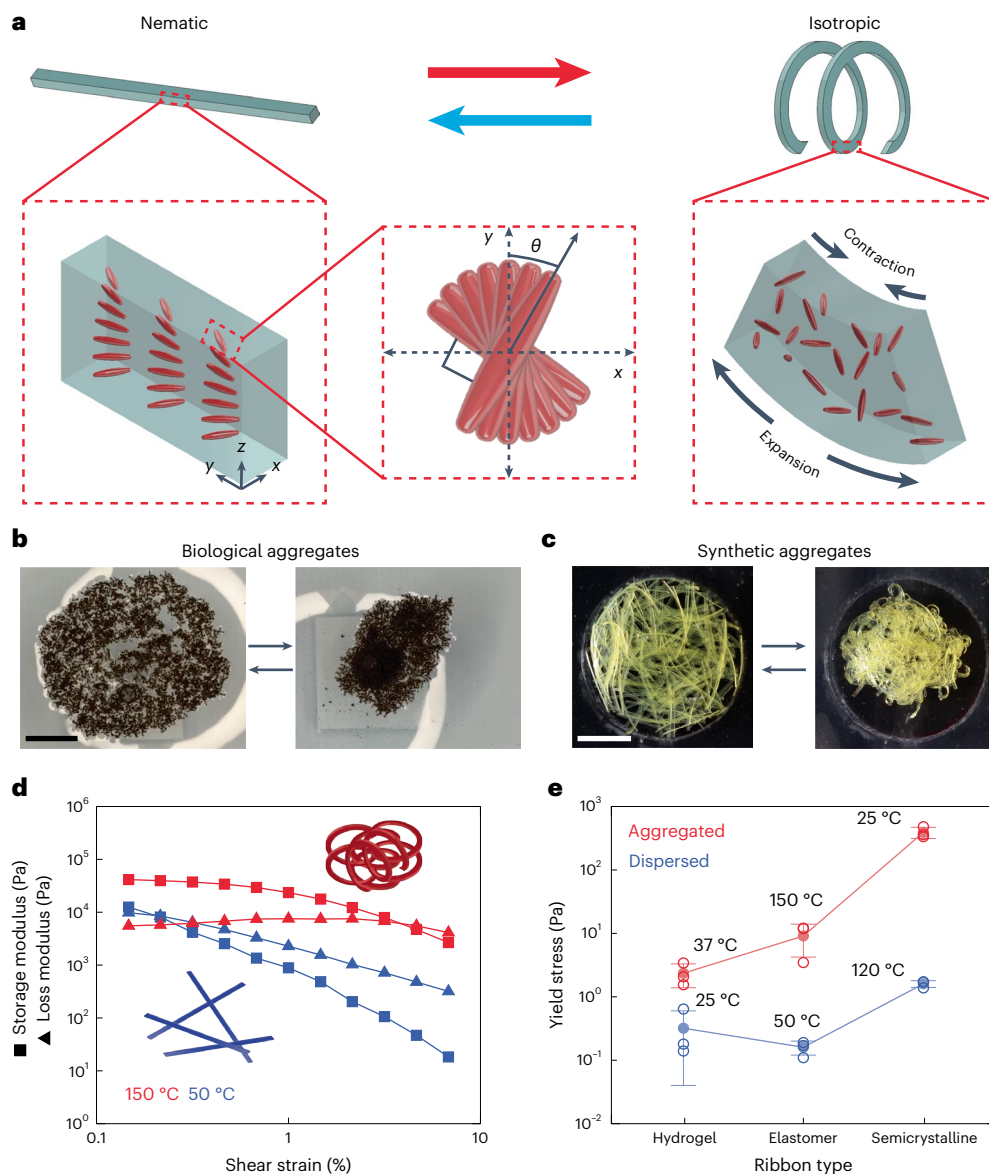
**Fig. 1 | Inspiration and construction of synthetic aggregates. a**, Schematic illustrating the mechanism that drives shape change in LCEs. An initially straight ribbon having a 90° transition in the orientation of the nematic director from the bottom surface to the top surface of the ribbon and angle $\theta$ between the ribbons' longitudinal axis and the orientation of the nematic director on the top surface **b**, Top view of a biological system consisting of fire ants (*S. invicta*) undergoing global volumetric contraction. Scale bar, 20 mm. **c**, Top view of a synthetic system consisting of LCE ribbons, with a length of 6 mm and an offset angle of 10°, submerged in silicone oil at a ribbon packing density of 0.075 mg mm⁻³ transitioning from dispersed to aggregated after being heated from 25 to 175 °C.

Scale bar, 5 mm. **d**, Representative graph of oscillatory rheology strain sweeps plotting the storage modulus and loss modulus as a function of shear strain of ribbons with a length of 6 mm and offset angle $\theta = 10°$ at an initial density of 0.075 mg mm⁻³. **e**, Yield stress plotted as a function of ribbon type at the aggregated (red) and dispersed (blue) state. Data are presented as individual data points and mean values ± standard deviation (s.d.). The hollow circles represent individual data points, the solid circles represent the mean and the error bars represent the standard deviation. $N = 3$. All the ribbons were loaded at an initial packing density of 0.03 mg mm⁻³. Hydrogel ribbons were dispersed in water, whereas elastomers and semicrystalline ribbons were dispersed in silicone oil.

aggregates comprising longer ribbons achieve more entanglements per ribbon, thus increasing their penetration resistance and yield stresses.

In addition to ribbon length, the ribbon offset angle also influences the aggregate mechanics (Supplementary Note 3). An offset angle of 0° induces pure bending, and an offset angle of 45° leads to pure twisting. Offset angles between 0° and 45° lead to some combinations of bending and twisting (Fig. 2e and Supplementary Fig. 2). Although aggregation occurs for ribbons with offset angles of 0° or 10°, ribbons with a 45° offset do not cohere and exhibit a negligible change in mechanical properties with temperature (Fig. 2f–h and Supplementary Figs. 11 and 12). As the offset angle is increased from 0° to 10°, the yield stress of the aggregates decreases from 516 ± 162 Pa (at

5.36 ± 1.25% strain) to 300 ± 50 Pa (at 4.15 ± 0.04% strain) (Fig. 2f, g). After cooling, the yield stress decreases to 36 ± 4 Pa (at 0.30 ± 0.03% strain) and 25 ± 5 Pa (at 0.19 ± 0.04% strain) for 0° and 10° ribbons, respectively (Fig. 2g and Supplementary Fig. 12). The decrease in yield stress with respect to increasing offset angle suggests that bending, and not twisting, is the requisite geometric trait required to induce entanglement in these aggregates. We note the values in yield stress between the heated and cooled dispersions of both 0° ($p = 0.01$, $n = 3$, paired *t*-test) and 10° ($p = 0.04$, $n = 3$, paired *t*-test) ribbons are significantly different; however, no significant difference in yield stress is observed for 45° ($p = 0.20$, $n = 3$, paired *t*-test) ribbons (Supplementary Fig. 13).
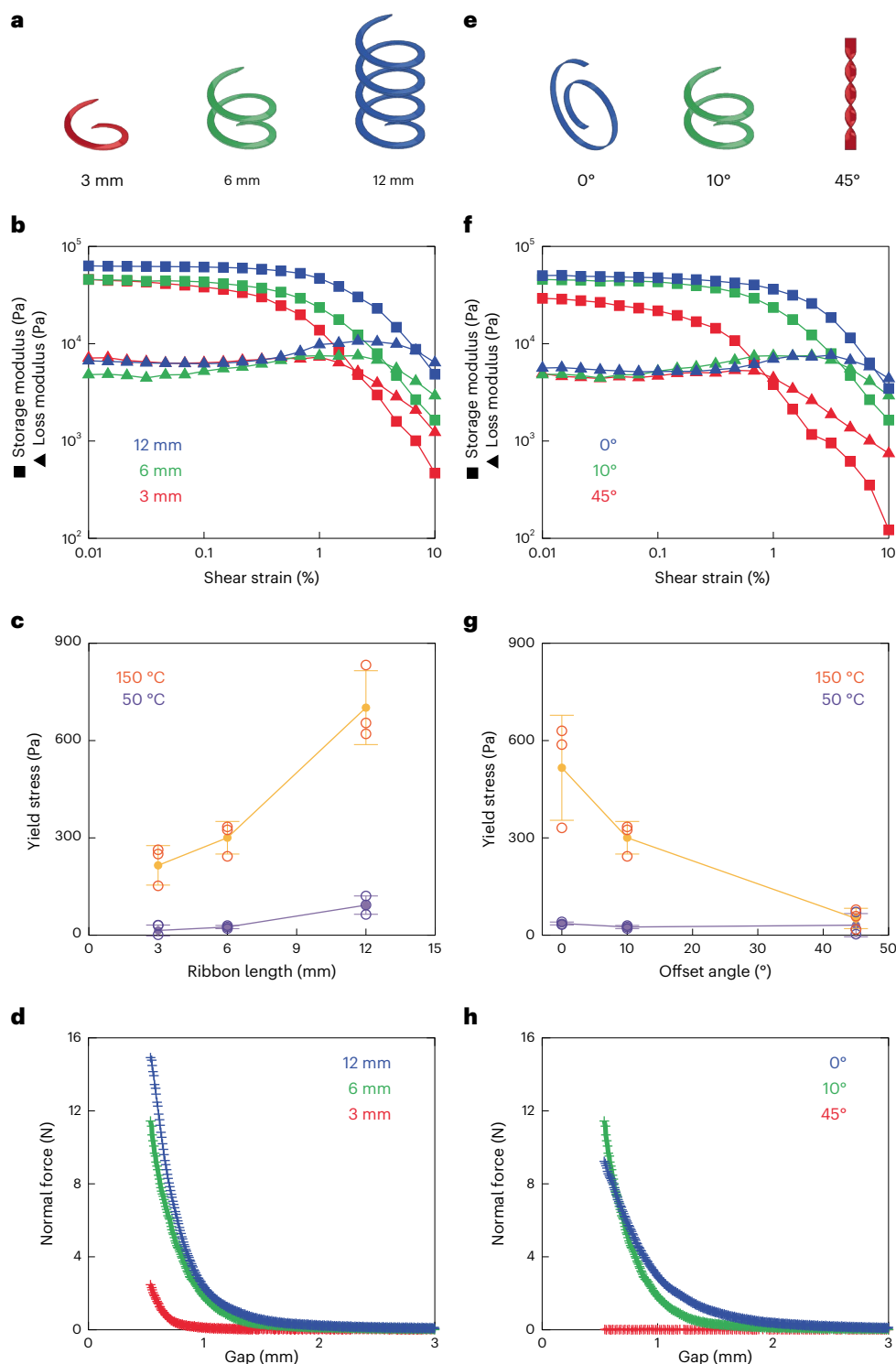
**Fig. 2 | Individual ribbon parameters affect global mechanical properties.**
**a**, Schematic of individual ribbons with varying lengths in their heated, actuated state. The offset angle for ribbons is 10°. **b**, Representative graph of oscillatory rheology strain sweeps ($\omega = 10$ rad s$^{-1}$) plotting the storage modulus and loss modulus as a function of shear strain in the heated, aggregated state of ribbons with varying lengths and having an offset angle of 10°. **c**, Yield stress plotted as a function of ribbon length at 150 °C (orange) and after cooling to 50 °C (purple). The hollow circles represent individual data points, the solid circles represent the mean and the error bars represent the standard deviation. $N = 3$. The offset angle of ribbons is 10°. **d**, Representative graph plotting the normal force as a function of gap for penetration tests of aggregates comprising ribbons with different lengths and an offset angle of 10°. **e**, Schematic of individual ribbons with varying

offset angles in their heated, actuated state. The length of ribbons is 6 mm.
**f**, Representative graph of oscillatory rheology strain sweeps ($\omega = 10$ rad s$^{-1}$) plotting the storage modulus and loss modulus as a function of shear strain in the heated state of ribbons with varying offset angles and a length of 6 mm. **g**, Yield stress plotted as a function of offset angle at 150 °C (orange) and after cooling to 50 °C (purple). The hollow circles represent individual data points, the solid circles represent the mean and the error bars represent the standard deviation. $N = 3$. The length of ribbons is 6 mm. **h**, Representative graph plotting the normal force as a function of gap for penetration tests in the heated state of a dispersion of ribbons with varied offset angles and a length of 6 mm. All the experiments were conducted at a ribbon packing density of 0.075 mg mm$^{-3}$. The error bars represent the standard deviation. $N = 3$.
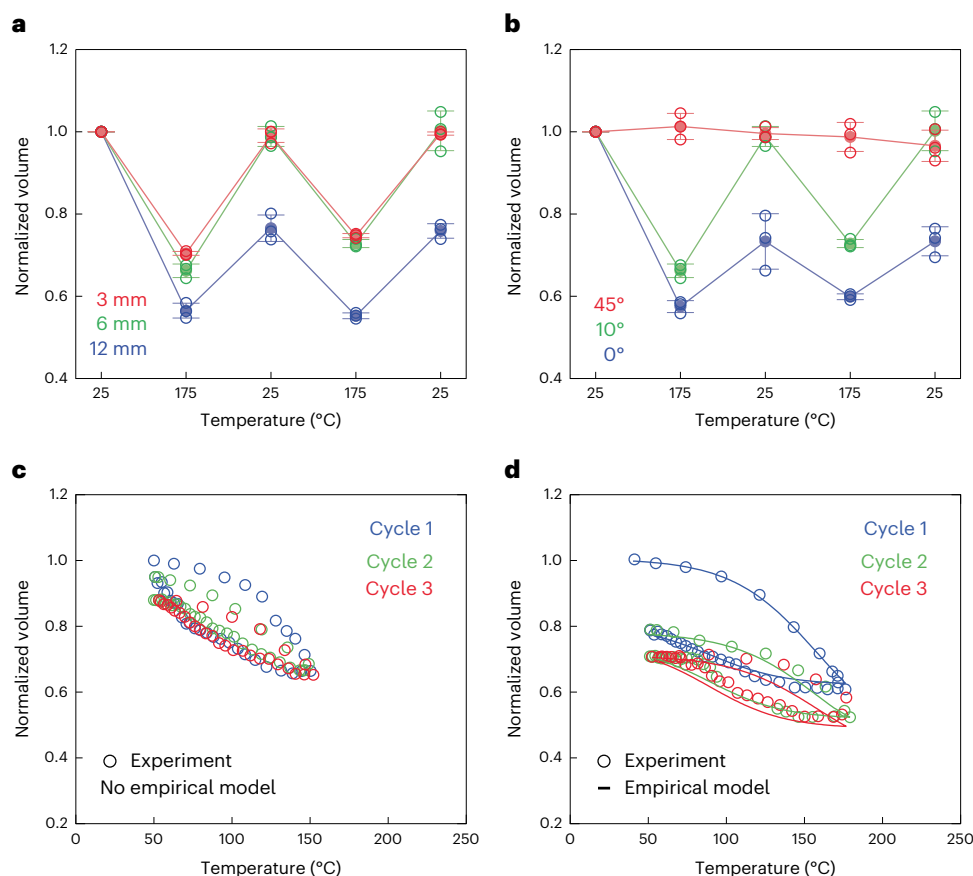
**Fig. 3 | Contractile reversibility. a**, Normalized volume plotted as a function of temperature cycled from 25 to 175 °C of 3 mm ribbons (red), 6 mm ribbons (green) and 12 mm ribbons (blue). The offset angle of ribbons is 10°. The hollow circles represent individual data points, the solid circles represent the mean and the error bars represent the standard deviation. N = 3. **b**, Normalized volume plotted as a function of temperature cycled from 25 to 175 °C of ribbons with varied offset angles. The length of the ribbons is 6 mm. The hollow circles represent individual data points, the solid circles represent the mean and the error bars represent the standard deviation. N = 3. **c**, Normalized volume plotted as a function of temperature for a dispersion of 12 mm ribbons, having an offset angle of 10°, cyclically heated and cooled from 50 to 150 °C. The circles indicate the experimental data. The blue circles indicate the first cycle, the green circles indicate the second cycle and the red circles indicate the third cycle. **d**, Normalized volume plotted as a function of temperature for a dispersion of 12 mm ribbons, having an offset angle of 10°, cyclically heated and cooled from 50 to 175 °C. The solid line indicates the empirical model and the circles indicate the experimental data. The blue curves indicate the first cycle, the green curves indicate the second cycle and the red curves indicate the third cycle. All the experiments were conducted at a ribbon packing density of 0.075 mg mm⁻³.

## Aggregation reversibility is governed by ribbon actuation

Ribbon length and offset angle impact the degree of volumetric contraction and reversibility of the aggregate. Ribbons of varying lengths and 10° offset angle were placed into a well with a packing density of 0.075 mg mm$^{-3}$ and subjected to two heating and cooling cycles. The volume enveloped by the aggregates was measured with respect to temperature. Initially, at room temperature, dispersed ribbons occupied the entire volume of the well. However, after heating, the aggregates comprising 3-, 6- and 12-mm-long ribbons contracted to 70.41 ± 0.49%, 66.21 ± 1.65% and 56.50 ± 1.82% of their original volume, respectively (Fig. 3a). Although aggregates comprising the 3 and 6 mm ribbons fully redisperse after cooling, the 12 mm ribbon only returned to 76.56 ± 3.23% of its original volume when cooled. Although the greater degree of volumetric contraction for the 12 mm ribbons is perhaps indicative of higher entanglement density, the inability to disperse on cooling is indicative of entanglement irreversibility. Ribbons of varying offset angles and 6 mm length were also placed in wells at the same packing density and subjected to the same thermal cycling (Fig. 3b). Although ribbons with a 45° offset exhibited negligible thermal contraction, ribbons with a 10° offset exhibited fully reversible contraction

and expansion. However, ribbons with a 0° offset (that is, no twist) only occupy 73.0 ± 6.7% of the initial volume after their first heating and cooling cycle, again suggesting entanglement irreversibility. Importantly, irreversibility is not observed in individual ribbons undergoing the same thermal loading (Supplementary Fig. 14), affirming topological changes as the source of aggregate irreversibility.

To quantify the degree of reversibility as well as its temperature dependence, we employ a simple empirical model and find that the normalized volume evolves with temperature following a modified logistic function (Supplementary Note 4 and Supplementary Figs. 15–18). We deduce the approximate threshold for reversibility by cyclically heating a dispersion of 12 mm ribbons between 50 and 150 °C (Fig. 3c). As these thermal conditions yielded nearly fully reversible aggregates, we deduced that the reversibility threshold is on the order of 0.67 ± 0.02. We leverage this approximate threshold and use it as a fitting parameter for each cycle of the system heated to 175 °C. Fitting the equation with the data for 12 mm ribbons from Fig. 3a, we empirically model the cyclic behaviour of 12 mm ribbons heated between 50 and 175 °C (Fig. 3d). Therefore, aggregation reversibility is programmable through features such as ribbon length, ribbon offset angle and temperature.
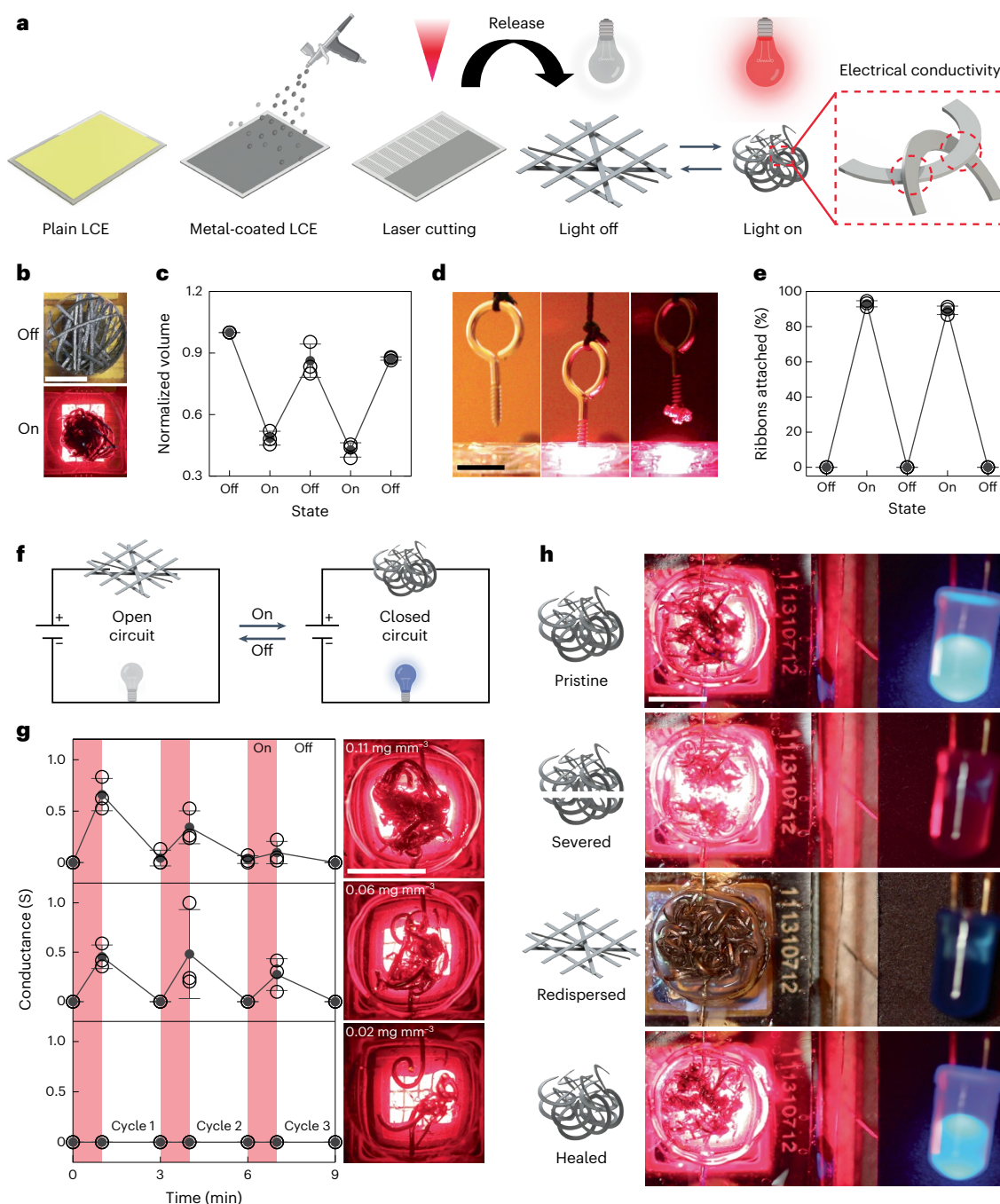
**Fig. 4 | Metal coating enables emergent functionalities. a**, Schematic illustrating the process of coating ribbons with a liquid metal, enabling NIR-responsive aggregates and conductive aggregates. **b**, Dispersion of coated ribbons with an offset angle of 10° and a length of 6 mm at a ribbon packing density of 0.075 mg mm$^{-3}$, aggregating in the presence of NIR light. Scale bar, 3 mm. **c**, Normalized volume plotted as a function of the NIR-light state of coated ribbons with an offset angle of 10° and a length of 6 mm at a packing density of 0.075 mg mm$^{-3}$ for three cycles. Data are presented as individual data points and mean values ± s.d. The hollow black circles represent individual data points, the solid grey circles represent the mean and the error bars represent the standard deviation. $N = 3$. **d**, Aggregation can be used to form a solid-like aggregate around a foreign object and latch on. Scale bar, 5 mm. **e**, Percentage of ribbons attached to the foreign object plotted as a function of the NIR-light state.

Data are presented as individual data points and mean values ± s.d. The hollow black circles represent individual data points, the solid grey circles represent the mean and the error bars represent the standard deviation. $N = 3$. **f**, Schematic illustrating that ribbons can transition from an insulating state to a conductive state depending on the state of NIR light. **g**, Conductance measured as a function of time for three cycles of turning the NIR light from off to on for three different packing densities. Scale bar, 8 mm. Data are presented as individual data points and mean values ± s.d. The hollow black circles represent individual data points, the solid grey circles represent the mean and the error bars represent the standard deviation. $N = 3$. **h**, Conductive aggregates are capable of healing damage by turning the light off and on. Note that the dispersed ribbons were manually stirred only for this experiment. Scale bar, 5 mm. The error bars represent the standard deviation. $N = 3$.

## Light-responsive and conductive aggregates

Coupling LCE ribbons with functional coatings enables multistimuli response and conductive aggregates (Fig. 4a)[44,45]. In the presence

of near-infrared (NIR) light, ribbons coated with a strain-tolerant metal coating[46] (Supplementary Fig. 19) demonstrate photother-mally induced shape change[44] and aggregation (Fig. 4b). The volume
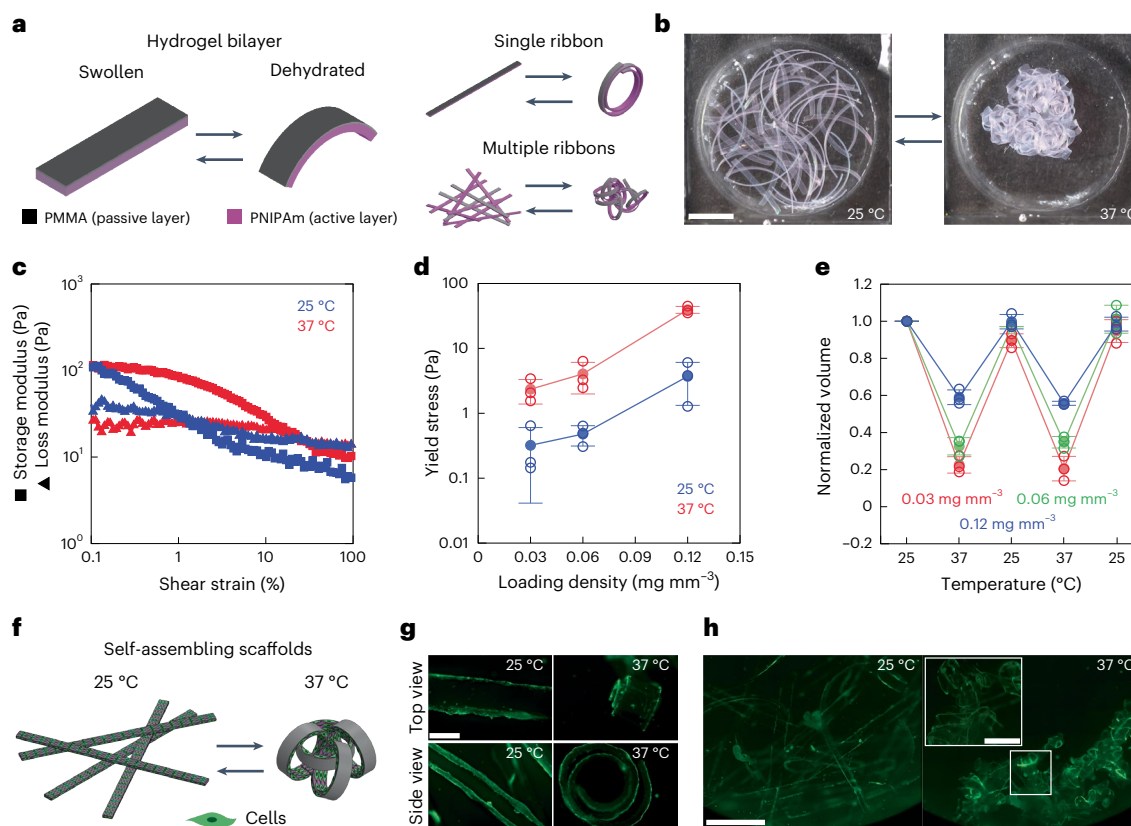
**Fig. 5 | Hydrogel ribbons enable aggregation in physiologically relevant conditions. a**, Schematic illustrating the mechanism of a single ribbon bending and multiple ribbons aggregating through a hydrogel bilayer system composed of a passive PMMA layer and an active poly(*N*-isopropylacrylamide) (PNIPAm) layer in response to heating-induced deswelling. **b**, Dispersion of hydrogel ribbons having a length of 10 mm and loaded at a density of 0.06 mg mm$^{-3}$ aggregating in response to heating from 25 to 37 °C. Scale bar, 5 mm. **c**, Representative graph of oscillatory rheology strain sweeps plotting the storage modulus and loss modulus as a function of shear strain of hydrogel ribbons, having a length of 10 mm at an initial loading density of 0.06 mg mm$^{-3}$. **d**, Yield stress plotted as a function of ribbon loading density at 37 °C (red) and after cooling to 25 °C (blue). Data are presented as individual data points and mean values ± s.d. The hollow circles represent individual data points, the solid circles represent the mean and the error bars represent the standard deviation. *N* = 3. The length of the ribbons is 10 mm. **e**, Normalized volume plotted as a function

of temperature cycled from 25 to 37 °C of ribbons loaded at an initial density of 0.03 mg mm$^{-3}$ (red), 0.06 mg mm$^{-3}$ (green) and 0.12 mg mm$^{-3}$ (blue). The length of the ribbons is 10 mm. Data are presented as individual data points and mean values ± s.d. The hollow circles represent individual data points, the solid circles represent the mean and the error bars represent the standard deviation. *N* = 3. **f**, Schematic illustrating the self-assembly of cell-seeded scaffolds through the use of bilayer hydrogel ribbon dispersions. **g**, Top and side views of the hydrogel ribbon seeded with mouse 3T3 fibroblasts demonstrating the transition from a straight to a bent configuration in response to heating from 25 to 37 °C. Scale bar, 500 μm. The experiment was repeated three times yielding similar results. **h**, Fluorescence micrograph of a dispersion of ribbons seeded with mouse 3T3 fibroblasts aggregating in response to increasing the temperature from 25 to 37 °C, demonstrating cell viability within an aggregate. Scale bar, 3 mm (inset, 1 mm). 3T3 fibroblasts were seeded on ribbons for three days before imaging. The experiment was repeated three times, yielding similar results.

occupied by the ribbons decreases to 49 ± 3% of its original value when exposed to NIR light and returns to 86 ± 8% of the original volume when the NIR light is switched off (Fig. 4c and Supplementary Video 4). Temporal control of volume change is used for collective grasping (Fig. 4d). When the light is off, a screw can be independently removed from a dispersion of coated LCE ribbons. However, when the light is on, the ribbons entangle, forming an aggregate around the screw; therefore, the removal of the screw leads to the removal of the aggregate. These aggregates are also capable of healing damage (Supplementary Fig. 20). On NIR-light exposure, the dispersed ribbons form an aggregate that is then severed. By toggling off the NIR light, stirring and then reintroducing NIR light, the ribbons redisperse and then reaggregate.

Mechanical entanglement of conductive ribbons leads to a reversible transition from electrically insulating to conducting (Fig. 4a,f). The conductance increases from 0 to 0.85 ± 0.14 S as the temperature is increased from 50 to 175 °C (Supplementary Fig. 21) and then decreases back to 0 after cooling (Supplementary Video 5). The ribbon packing density plays an important role in forming conductive pathways, as aggregates must be capable of attaching to both leads and maintain

structural integrity (Fig. 4g). At a low packing density of 0.02 mg mm$^{-3}$, the ribbons are incapable of achieving electrical continuity between the two fixed leads in response to photothermal heating. However, at a packing density of 0.06 mg mm$^{-3}$, the aggregates form a continuous network between leads, giving rise to a switchable soft conductor. On cyclic NIR illumination, the conductance initially increases from 0 to 0.45 ± 0.12 S in the presence of light, with an increase from 0 to 0.27 ± 0.16 S by the third cycle. At the highest packing density of 0.11 mg mm$^{-3}$, the conductance increases from 0 to 0.66 ± 0.16 S on irradiation; however, the residual conductance of 0.04 ± 0.08 S then occurs in the dark due to residual contacts between ribbons. By exploiting these aggregates' reprocessability and conductance, healable, photoresponsive electronic circuits are realized (Fig. 4h, Supplementary Fig. 22 and Supplementary Video 6).

## Aggregation near room temperature
The shape of the liquid crystal polymer networks depends not only on the temperature but also on the presence of the solvent. Liquid crystalline gels (LCGs) were synthesized to create aggregates that are

stable at room temperature. The swelling or deswelling of LCG films enables isothermal, programmed shape change used to irreversibly form aggregates stable at room temperature (Supplementary Note 5 and Supplementary Figs. 23–27)[47,48]. Reversible aggregates stable at room temperature are formed using semicrystalline liquid crystal polymer ribbons that are bent and twisted at room temperature and flat at elevated temperatures[39] (Supplementary Note 5 and Supplementary Figs. 28 and 29). Although semicrystalline LCEs enable reversible aggregates stable at room temperature, high temperatures are needed to redisperse the ribbons, which hinders the use of this mechanism for sensitive environments, such as biomedical applications.

Hydrogel bilayer ribbons enable the formation and dispersion of aggregates at lower temperatures and in water, thereby making them potentially well suited for biomedical applications. Individual ribbons are bilayers of a thermoresponsive hydrogel layer with a passive polymeric layer[49,50] (Fig. 5a and Supplementary Fig. 3). When a dispersion of these ribbons is suspended in water and heated, ribbons mechanically interlock and contract (Fig. 5b). At a higher temperature of 37 °C, a ribbon dispersion loaded at an initial packing density of 0.06 mg mm$^{-3}$ aggregates, exhibiting a yield stress of 4.03 ± 2.05 Pa at a yield strain of 16.44 ± 11.64%. After cooling, the ribbons redisperse and exhibit a yield stress of 0.48 ± 0.17 Pa at a yield strain of 1.38 ± 0.39% (Fig. 5c and Supplementary Figs. 30 and 31). Furthermore, the initial packing density and length of ribbons determine the aggregate formation and mechanical properties (Fig. 5d, Extended Data Fig. 1 and Supplementary Figs. 30–33). As the initial packing density of the dispersion increases from 0.03 to 0.06 and 0.12 mg mm$^{-3}$, the yield stress of the aggregate increases from 2.35 ± 0.96 Pa (at a strain of 12.37 ± 3.61%) to 4.03 ± 2.05 Pa (at a strain of 16.44 ± 11.64%) and 39.43 ± 4.82 Pa (at a strain of 48.97 ± 22.39%) (Fig. 5d and Supplementary Fig. 30). Along with aggregation-induced increases in yield stress and yield strain, ribbon dispersions also demonstrate a decrease in volume on heating (Fig. 5e and Supplementary Figs. 17, 18 and 34). The volume occupied by the aggregates decreases to 59.03 ± 3.96% at a loading density of 0.12 mg mm$^{-3}$, 32.59 ± 4.69% at a loading density of 0.06 mg mm$^{-3}$ and 22.57 ± 4.47% at a loading density of 0.03 mg mm$^{-3}$ (Fig. 5e).

Self-assembling scaffolds are made by seeding mouse 3T3 fibroblasts on planar hydrogel ribbons. Fibroblasts are seeded onto the ribbons by incorporating arginylglycylaspartic acid within the hydrogel layer (Fig. 5f)[51]. After cell culturing, fibroblasts can be found mainly along the ribbon edges, and individual ribbons transition from a straight to a bent configuration on heating to 37 °C (Fig. 5g). Dispersions of cell-coated ribbons, with high cell viability, transition into an aggregate in response to heating to 37 °C (Fig. 5h and Supplementary Figs. 35 and 36). The metabolic activity of the fibroblasts was maintained for at least ten days (Supplementary Fig. 37). Furthermore, responsive hydrogel ribbons may also be used as injectable blood-clotting agents due to their ability to self-assemble into porous structures with high surface areas[52]. Responsive hydrogel ribbons can induce a blood clot with no significant difference in time compared with the kaolin positive control (Supplementary Fig. 38). The clotting time of blood exposed to the bulk hydrogel is significantly longer than the blood-exposed hydrogel aggregate ($p = 0.0006$). The effect of surface area of a synthetic material on blood clotting is known[53]. However, the combination of injectability and self-assembled macroporosity that is enabled by entanglement is unique amongst previously described materials. This combination of properties allows the hydrogel ribbons to be injected, fill a model aneurysm and induce a blood clot (Supplementary Figs. 38 and 39).

## Summary and conclusions

We report a simple yet powerful method to create macroscopic aggregates capable of autonomous assembly and disassembly. Hydrogels, elastomers and semicrystalline ribbons are programmed to reversibly transition from straight to bent and twisted configurations in response to heating, NIR irradiation or presence of a solvent. By allowing multiple ribbons to actuate in proximity, the ribbons entangle and produce transient, viscoelastic solids. The initial packing density, shape and mechanical properties of the individual ribbons dictate the ability to form aggregates as well as the aggregate's mechanical properties. We introduce the parameters available for ribbon design and—through a combination of experimentation and stochastic simulations—predict and explain the onset of aggregation as a function of ribbon length, offset angle, loading temperature and packing density. Additionally, we examine the reversibility of aggregation and utilize an empirical model to explore the observed plasticity in a subset of these systems. Furthermore, coating ribbons with a liquid metal produces units that aggregate in response to NIR light and exhibit electrical conductance. Aggregation is a common trait in dispersions of stimuli-responsive ribbons. This may enable a wide range of materials to be assembled on demand, enabling a range of potential applications from stimuli-responsive circuits to injectable biomaterials.

## Online content

Any methods, additional references, Nature Portfolio reporting summaries, source data, extended data, supplementary information, acknowledgements, peer review information; details of author contributions and competing interests; and statements of data and code availability are available at https://doi.org/10.1038/s41563-023-01761-4.

## References

1. Diller, E., Zhang, N. & Sitti, M. Modular micro-robotic assembly through magnetic actuation and thermal bonding. *J. Micro-Bio Robot.* **8**, 121–131 (2013).
2. Yang, X., Tan, R., Lu, H., Fukuda, T. & Shen, Y. Milli-scale cellular robots that can reconfigure morphologies and behaviors simultaneously. *Nat. Commun.* **13**, 4156 (2022).
3. Fan, X., Dong, X., Karacakol, A. C., Xie, H. & Sitti, M. Reconfigurable multifunctional ferrofluid droplet robots. *Proc. Natl Acad. Sci. USA* **117**, 27916–27926 (2020).
4. Hu, D. L., Phonekeo, S., Altshuler, E. & Brochard-Wyart, F. Entangled active matter: from cells to ants. *Eur. Phys. J. Spec. Top.* **225**, 629–649 (2016).
5. Vernerey, F. J. et al. Biological active matter aggregates: inspiration for smart colloidal materials. *Adv. Colloid Interface Sci.* **263**, 38–51 (2019).
6. Metzmacher, J., Poty, M., Lumay, G. & Vandewalle, N. Self-assembly of smart mesoscopic objects. *Eur. Phys. J. E* **40**, 108 (2017).
7. Dierichs, K. & Menges, A. Towards an aggregate architecture: designed granular systems as programmable matter in architecture. *Granular Matter* **18**, 25 (2016).
8. Wagner, R. J., Such, K., Hobbs, E. & Vernerey, F. J. Treadmilling and dynamic protrusions in fire ant rafts. *J. R. Soc. Interface* **18**, 20210213 (2021).
9. Grozinger, C. M., Richards, J. & Mattila, H. R. From molecules to societies: mechanisms regulating swarming behavior in honey bees (*Apis* spp.). *Apidologie* **45**, 327–346 (2014).
10. Patil, V. P. et al. Ultrafast reversible self-assembly of living tangled matter. *Science* **380**, 392–398 (2023).
11. Mlot, N. J., Tovey, C. A. & Hu, D. L. Fire ants self-assemble into waterproof rafts to survive floods. *Proc. Natl. Acad. Sci. USA* **108**, 7669–7673 (2011).
12. Anderson, C., Theraulaz, G. & Deneubourg, J.-L. Self-assemblages in insect societies. *Insect Soc.* **49**, 99–110 (2002).
13. Ozkan-Aydin, Y., Goldman, D. I. & Bhamla, M. S. Collective dynamics in entangled worm and robot blobs. *Proc. Natl. Acad. Sci. USA* **118**, e2010542118 (2021).
14. Tennenbaum, M., Liu, Z., Hu, D. & Fernandez-Nieves, A. Mechanics of fire ant aggregations. *Nat. Mater.* **15**, 54–59 (2016).

15. Foster, P. C., Mlot, N. J., Lin, A. & Hu, D. L. Fire ants actively control spacing and orientation within self-assemblages. *J. Exp. Biol.* **217**, 2089–2100 (2014).

16. Tennenbaum, M. & Fernandez-Nieves, A. Activity-driven changes in the mechanical properties of fire ant aggregations. *Phys. Rev. E* **96**, 052601 (2017).

17. Deblais, A., Woutersen, S. & Bonn, D. Rheology of entangled active polymer-like *T. tubifex* worms. *Phys. Rev. Lett.* **124**, 188002 (2020).

18. Weiner, N., Bhosale, Y., Gazzola, M. & King, H. Mechanics of randomly packed filaments—the 'bird nest' as meta-material. *J. Appl. Phys.* **127**, 050902 (2020).

19. Mezeix, L., Bouvet, C., Huez, J. & Poquillon, D. Mechanical behavior of entangled fibers and entangled cross-linked fibers during compression. *J. Mater. Sci.* **44**, 3652–3661 (2009).

20. Rodney, D., Gadot, B., Martinez, O. R., Roscoat, S. Rdu & Orgéas, L. Reversible dilatancy in entangled single-wire materials. *Nat. Mater.* **15**, 72–77 (2016).

21. Murphy, K. A., Reiser, N., Choksy, D., Singer, C. E. & Jaeger, H. M. Freestanding loadbearing structures with Z-shaped particles. *Granular Matter* **18**, 26 (2016).

22. Xin, S., Chimene, D., Garza, J. E., Gaharwar, A. K. & Alge, D. L. Clickable PEG hydrogel microspheres as building blocks for 3D bioprinting. *Biomater. Sci.* **7**, 1179–1187 (2019).

23. Muir, V. G. et al. Sticking together: injectable granular hydrogels with increased functionality via dynamic covalent inter-particle crosslinking. *Small* **18**, e2201115 (2022).

24. Buttinoni, I. et al. Dynamical clustering and phase separation in suspensions of self-propelled colloidal particles. *Phys. Rev. Lett.* **110**, 238301 (2013).

25. Lazarus, C., Pouliopoulos, A. N., Tinguely, M., Garbin, V. & Choi, J. J. Clustering dynamics of microbubbles exposed to low-pressure 1-MHz ultrasound. *J. Acoust. Soc. Am.* **142**, 3135–3146 (2017).

26. Xie, H. et al. Reconfigurable magnetic microrobot swarm: multimode transformation, locomotion, and manipulation. *Sci. Robot.* **4**, eaav8006 (2019).

27. Yan, J. et al. Reconfiguring active particles by electrostatic imbalance. *Nat. Mater.* **15**, 1095–1099 (2016).

28. Lin, Z. et al. Light-activated active colloid ribbons. *Angew. Chem.* **129**, 13702–13705 (2017).

29. Kessel, B. et al. 3D bioprinting of macroporous materials based on entangled hydrogel microstrands. *Adv. Sci.* **7**, 2001419 (2020).

30. Behl, M., Kratz, K., Zotzmann, J., Nöchel, U. & Lendlein, A. Reversible bidirectional shape-memory polymers. *Adv. Mater.* **25**, 4466–4469 (2013).

31. Gladman, A. S., Matsumoto, E. A., Nuzzo, R. G., Mahadevan, L. & Lewis, J. A. Biomimetic 4D printing. *Nat. Mater.* **15**, 413–418 (2015).

32. Yakacki, C. M. et al. Tailorable and programmable liquid-crystalline elastomers using a two-stage thiol–acrylate reaction. *RSC Adv.* **5**, 18997–19001 (2015).

33. Sawa, Y. et al. Shape selection of twist-nematic-elastomer ribbons. *Proc. Natl. Acad. Sci. USA* **108**, 6364–6368 (2011).

34. Lee, K. M., Bunning, T. J. & White, T. J. Autonomous, hands-free shape memory in glassy, liquid crystalline polymer networks. *Adv. Mater.* **24**, 2839–2843 (2012).

35. Zhao, Y. et al. Twisting for soft intelligent autonomous robot in unstructured environments. *Proc. Natl. Acad. Sci. USA* **119**, e2200265119 (2022).

36. Zhang, Y. et al. Seamless multimaterial 3D liquid-crystalline elastomer actuators for next-generation entirely soft robots. *Sci. Adv.* **6**, eaay8606 (2020).

37. Haan, L. T., de, Schenning, A. P. H. J. & Broer, D. J. Programmed morphing of liquid crystal networks. *Polymer* **55**, 5885–5896 (2014).

38. Wagner, R. J. & Vernerey, F. J. Computational exploration of treadmilling and protrusion growth observed in fire ant rafts. *PLoS Comput. Biol.* **18**, e1009869 (2022).

39. Javed, M. et al. Programmable shape change in semicrystalline liquid crystal elastomers. *ACS Appl. Mater. Interfaces* **14**, 35087–35096 (2022).

40. Cook, M. T., Haddow, P., Kirton, S. B. & McAuley, W. J. Polymers exhibiting lower critical solution temperatures as a route to thermoreversible gelators for healthcare. *Adv. Funct. Mater.* **31**, 2008123 (2021).

41. Wang, Q. et al. Lightweight mechanical metamaterials with tunable negative thermal expansion. *Phys. Rev. Lett.* **117**, 175901 (2016).

42. Minh, N. H. & Cheng, Y. P. On the contact force distributions of granular mixtures under 1D-compression. *Granular Matter* **18**, 18 (2016).

43. Liu, A. J. & Nagel, S. R. The jamming transition and the marginally jammed solid. *Annu. Rev. Condens. Matter Phys.* **1**, 347–369 (2010).

44. Chechetka, S. A. et al. Light-driven liquid metal nanotransformers for biomedical theranostics. *Nat. Commun.* **8**, 15432 (2017).

45. Ford, M. J. et al. A multifunctional shape-morphing elastomer with liquid metal inclusions. *Proc. Natl. Acad. Sci. USA* **116**, 21438–21444 (2019).

46. Tavakoli, M. et al. EGaIn-assisted room-temperature sintering of silver nanoparticles for stretchable, inkjet-printed, thin-film electronics. *Adv. Mater.* **30**, 1801852 (2018).

47. Urayama, K., Okuno, Y. & Kohjiya, S. Volume transition of liquid crystalline gels in isotropic solvents. *Macromolecules* **36**, 6229–6234 (2003).

48. Gelebart, A. H. et al. Photoresponsive sponge-like coating for on-demand liquid release. *Adv. Funct. Mater.* **28**, 1705942 (2018).

49. Yao, C. et al. Poly(*N*-isopropylacrylamide)-clay nanocomposite hydrogels with responsive bending property as temperature-controlled manipulators. *Adv. Funct. Mater.* **25**, 2980–2991 (2015).

50. Zhang, J., Zheng, L., Wu, Z., Wang, L. & Li, Y. Thermoresponsive bilayer hydrogel with switchable bending directions as soft actuator. *Polymer* **253**, 124998 (2022).

51. Shu, X. Z. et al. Attachment and spreading of fibroblasts on an RGD peptide–modified injectable hyaluronan hydrogel. *J. Biomed. Mater. Res. A* **68A**, 365–375 (2004).

52. Beaman, H. T. et al. Hemostatic shape memory polymer foams with improved survival in a lethal traumatic hemorrhage model. *Acta Biomater.* **137**, 112–123 (2022).

53. Landsman, T. L. et al. Design and verification of a shape memory polymer peripheral occlusion device. *J. Mech. Behav. Biomed. Mater.* **63**, 195–206 (2016).

## Methods

### Materials

Liquid crystal monomers 1,4-bis-[4-(6-acryloyloxyhexyloxy)benzoyloxy]-2-methylbenzene (RM82) and 1,4-bis-[4-(3-acryloyloxypropyloxy) benzoyloxy]-2-methylbenzene (RM257) were purchased from Wilshire Technologies. The liquid crystal monomer 1,4-phenylene bis(4-(hex-5-enyloxy)benzoate) was purchased from SYNTHON Chemicals. The low-molecular-weight liquid crystal 4-cyano-4′-pentylbiphenyl, photoinitiators Irgacure I-369 and Irgacure I-651, chain extender $n$-butylamine, the metals gallium and indium and polymethyl methacrylate (PMMA) were purchased from Fisher Scientific. Pentaerythritol tetrakis(3-mercaptopropionate), 2,2′-(ethylenedioxy) diethanethiol, $n$-isopropylacrylamide, poly(ethylene glycol), photoalignable dye, brilliant yellow, kaolin, Irgacure 2959, gelatin (type A, 300 Bloom), gelatin (type A, 80-300 Bloom) and methacrylic anhydride were purchased from Sigma-Aldrich. Lithium phenyl-2,4,6-trimethylbenzoylphosphinate was purchased from TCI America. Methacryloxyethyl thiocarbamoyl rhodamine B was purchased from Alfa Chemistry. Sudan IV powder dye was purchased from Alfa Aesar. Calcium chloride was purchased from Avantor. A two-part polydimethylsiloxane (PDMS) elastomer was purchased from Ellsworth Adhesives. Silver ink (JS-A102A, Metalon) was purchased from Novacentrix Cell and the adhesive peptide arginylglycylaspartic acid was purchased from GenScript (RP20297).

### Materials synthesis

Clean glass slides (VWR) with dimensions of 50 mm × 75 mm × 1 mm were subjected to $O_2$ plasma for 5 min. Subsequently, the slides were spin-coated with 1 wt% brilliant yellow in a dimethylformamide solution at a spin speed of 3,000 r.p.m. for 30 s. The slides were baked for 30 min at 90 °C on a hotplate to ensure the evaporation of dimethylformamide. Each coated glass slide was exposed to linearly polarized broadband visible light from a modified projector at an intensity of 10 mW cm$^2$ for 3 min to align the brilliant yellow molecules. After alignment, the coated glass slides were spin-coated at a speed of 3,000 r.p.m. for 30 s with a 9 wt% RM257 (reactive mesogens) and 1 wt% I-651 (photoinitiator) toluene solution (10 wt% solids). The slides were then irradiated with 365 nm ultraviolet (UV) light at an intensity of 2 mW cm$^{-2}$ for 5 min using a UV oven (UVP Crosslinker CL-3000) for polymerization. Glass cells were prepared by adhering a pair of RM257-coated glass slides together using a 50 μm spacer (USA Sealing) and superglue (498, Loctite). A 1.4:1.0 molar ratio of RM82 to $n$-butylamine was heated and mixed with 1.5 wt% of I-369. The solution was then allowed to partially fill the glass cell through capillary action on a hotplate at 75 °C before placing it in an oven at 75 °C to complete the filling and oligomerization. After 15 h of oligomerization, the glass cells were allowed to cool to room temperature before exposing the cell to 365 nm UV light (Lumen Dynamics, OmniCure LX400+) at an intensity of 8 mW cm$^{-2}$ for polymerization for 5 min on each side. After polymerization, the top glass slide was released, and the film was cut using a $CO_2$ laser cutter (Gravograph $CO_2$ laser LS100-40W). Supplementary Information provides additional information on materials synthesis.

### Mechanical characterization

To measure the rheological properties of aggregates or dispersions, previously reported experiments were followed with modification[14,17]. Briefly, parallel-plate rheological scans were conducted utilizing a rheometer (Anton Paar Physica MCR 301). A PDMS well was placed on the base to contain the ribbons and silicone oil in the rheometer (Supplementary Fig. 40). Sandpaper was adhered to the base of the PDMS well as well as the top plate (diameter, 8 mm) to minimize slipping. LCE ribbons were placed in silicone oil at a packing density of 0.075 mg mm$^{-3}$ and heated to 150 °C. The temperature was checked using a thermocouple (Traceable 4015CC). Oscillatory strain sweeps at an angular frequency rate of 10 rad s$^{-1}$ with a gap of 3.5 mm were performed for measuring the storage and loss moduli as a function of shear strain from 0.01% to 10.00%. The samples were then cooled to

50 °C, and the temperature was checked using a thermocouple. The same oscillatory strain sweeps were performed at a lower temperature. No external manipulation of the sample occurred between these tests. The rheological properties of semicrystalline LCE ribbons were conducted in a similar manner as above. Ribbons were placed in a well with silicone oil heated to 120 °C loaded at an initial packing fraction of 0.03 mg mm$^{-3}$. After loading, the ribbons were cooled to 25 °C to form the aggregates. After aggregation, oscillatory strain sweeps at an angular frequency rate of 10 rad s$^{-1}$ with a gap of 3.5 mm were performed for measuring the storage and loss moduli as a function of shear strain from 0.01% to 100.00%. The samples were then reheated to 120 °C, and the temperature was checked using a thermocouple. The same oscillatory strain sweeps were performed at a higher temperature. No external manipulation of the sample occurred between these tests. The rheological properties of the hydrogels were performed in a similar manner to the LCEs; however, the ribbons were dispersed in water heated to 37 °C before conducting oscillatory strain sweeps at an angular frequency rate of 1 rad s$^{-1}$ with a gap of 3.5 mm as a function of shear strain from 0.01% to 100.00%. The yield stress and yield strain values were measured as the shear stress and strain value at the cross-over point between the loss modulus and storage modulus[54,55]. Three separate batches of ribbons were tested for each condition.

Penetration tests were performed using a rheometer (Anton Paar Physica MCR 301) by replacing the top plate with a cylindrical penetration probe with a diameter of 2.5 mm. A cylindrical PDMS well of dimensions (diameter, 10 mm; height, 3 mm) was placed on the base to contain the ribbons and silicone oil in the rheometer (Supplementary Fig. 40). The ribbons were dispersed in silicone oil at a packing density of 0.075 mg mm$^{-3}$. The top of the PDMS well was covered with a glass slide to mould the ribbons into a puck geometry and heating to 150 °C. The temperature was checked using a thermocouple. After reaching 150 °C, the top glass slide was removed, and the probe penetrated the sample at a rate of 100 μm s$^{-1}$. The normal force was measured as a function of the gap. After performing the test, the probe was extracted from the sample, and the sample was allowed to cool to 50 °C. After cooling, the test was performed under the same conditions. Penetration tests of hydrogels were performed in a similar manner, except that the samples were heated to 37 °C and loaded in water instead of silicone oil. No external manipulation of the sample occurred between these tests. Three separate batches of LCE ribbons were tested for each ribbon shape using the same testing conditions.

Tensile tests of semicrystalline LCE aggregates were performed by moulding the samples into a rectangular prism. A PDMS well that contained a void with a length of 15 mm, a width of 10 mm and a depth of 5 mm was fabricated through replica moulding of a 3D-printed part. Ribbons, having an offset angle of 10°, were dispersed into the PDMS well containing silicone oil at an initial loading density of 0.03 mg mm$^{-3}$. The bath was heated to 120 °C and the temperature was measured using a thermocouple. After reaching 120 °C, the ribbons were cooled to 25 °C to develop the aggregates. After the aggregates were created, silicone oil was removed by submerging the aggregates into isopropyl alcohol and rinsing with isopropyl alcohol. After washing, the aggregates were dried for 4 h in an oven set at 37 °C. After drying, the aggregates were loaded into a dynamic mechanical analyzer ((TA Instruments, RSA-G2). Stress was measured as a function of strain at a strain rate of 0.1 mm s$^{-1}$. The tests were conducted on three separate samples from three separate semicrystalline LCEs.

### Volume change

The relative volume changes of the aggregates composed of LCE ribbons were measured by placing the ribbons in a PDMS well with a diameter of 16 mm and a depth of 5 mm. The ribbons were observed to largely be oriented normal to the thickness of the cylindrical mould. A glass slide was placed on top of the well to encapsulate the ribbons. The ribbons were imaged at an initial temperature of 25 °C and a heated temperature of 175 °C. Three thermal cycles were performed. The images were analysed

using ImageJ software (version 1.53t). Three separate batches of LCE ribbons were tested for each ribbon shape using the same testing conditions. To measure the volume as a function of temperature, the experiments were conducted in a similar manner; however, synchronized video recordings were taken of the temperature readout of the thermocouple as well as the volume change of the aggregate. Supplementary Information provides additional information on aggregate volume change.

## Monte Carlo simulation

The Monte Carlo simulation was developed in two dimensions using MATLAB (MathWorks) based on the observation that the ribbons roughly occupy a two-dimensional plane when placed into the cylindrical wells used in the experiments and the assumption that ribbons were approximately evenly spatially distributed. The simulation first defines a discretized grid with a prescribed planar concentration $c$. It then seeds the 'ribbons' of length $L$, so that one ribbon is centred on every grid point. Each ribbon, which is straight to represent the geometry of real ribbons at room temperature, is then prescribed a random angle in the uniform range of $[0, \pi]$ rad. The networks are then visually plotted and then image analysis is conducted to determine if the straight ribbons form a fully percolated overlapping two-dimensional network.

## Photothermal response

Liquid-metal-coated ribbons demonstrate a photothermal response. To analyse NIR-light-driven aggregation, a circular PDMS well, having a diameter of 6 mm and a depth of 5 mm, was placed on top of an NIR-light source at a distance of 1 mm. The coated ribbons, having a length of 6 mm and an offset angle of 10°, were dispersed in silicone oil and placed in the well at a packing density of 0.075 mg mm$^{-3}$. A glass slide was placed on top of the well to encapsulate the ribbons. A 735 nm NIR light-emitting diode (LED) (CBM-120-FR Luminus Devices) was used to illuminate the sample from the bottom. The NIR LED was powered through a laboratory-grade d.c. power supply with current and voltage adjustment capabilities (Extech). The intensity of the NIR LED was 42 mW mm$^{-2}$ at the bottom of the well. A camera was placed on top of the setup to image the volume change. The image was taken before NIR-light illumination. NIR light illuminated the sample for 30 s, and the sample was imaged. The NIR light was turned off for 90 s, and the sample was imaged. This cycle was repeated twice. The images were analysed using ImageJ software. Three separate batches of coated LCE ribbons were tested.

## Conductance

Measuring the conductance of coated ribbons was performed using ambient heating and NIR-light exposure. To measure the conductance through ambient heating, coated ribbons (length, 6 mm; offset angle, 10°) were dispersed in a circular PDMS well, having a diameter of 16 mm and a depth of 5 mm, at a packing density of 0.075 mg mm$^{-3}$. Within the PDMS well, the ribbons were dispersed around two copper wire leads spread 5 mm apart that were attached to a multimeter (Fluke 114 electrical multimeter). A thermocouple (Traceable 4015CC) was inserted into the well to measure the temperature. To measure the resistance (R) as a function of temperature, synchronized video recordings were taken of the temperature readout of the thermocouple, the resistance readout of the multimeter and the ribbon dispersion. The conductance (G) was calculated using the following formula:

$$G = \frac{1}{R}$$

To measure the conductance of coated ribbons using NIR light, a similar testing procedure was used; however, to ensure the flood exposure of NIR light, the diameter of the circular well was reduced to 10 mm. Additionally, to understand the effect of packing density on conductance, three different ribbon packing densities were used: 0.02, 0.06 and 0.11 mg mm$^{-3}$. The samples were cyclically exposed to NIR at a timeframe of 1 min on, 2 min off. The intensity of NIR light was 42 mW mm$^{-2}$. The resistance values were collected at the end of each timeframe. Three separate batches of coated LCE ribbons were tested using the same experimental setup for both heat-induced conductance and NIR-light-induced conductance.

## Moulding

The LCGs were used to mould structures capable of maintaining their shape at room temperature. Briefly, LCG ribbons were placed in a vial containing silicone oil. Ribbons and silicone oil were drop cast into a PDMS negative mould created by moulding from a 3D-printed part. Once the LCG ribbons filled the mould, the entire structure was heated to 150 °C. As the LCG ribbons are heated, the 4-cyano-4′-pentylbiphenyl solvent is released from the system, causing them to irreversibly deswell and change shape in a way that is similar to heating an LCE ribbon. Once cooled back to room temperature, the moulded structure was released. Due to the loss of solvent, the structure maintains its integrity. After releasing, the structure was submerged in an isopropyl alcohol bath and rinsed with isopropyl alcohol to wash off the silicone oil. The structure was then allowed to dry for 4 h in an oven set at 37 °C before weighing. The density of the moulded structure was 0.12 mg mm$^{-3}$, as calculated by dividing the mass of the moulded structure by the internal volume of the mould used. Supplementary Information provides additional information on aggregate moulding.

## Aggregate reformation after damage

The reformation of aggregates after structural damage was performed using both LCE ribbons and metal-coated LCE ribbons. The reformation of LCE aggregates was performed by initially dispersing the LCE ribbons, having an offset angle of 10° and length of 6 mm, into a silicone oil bath at an initial packing density of 0.075 mg mm$^{-3}$. The LCE ribbons and silicone oil were contained in a PDMS well that has a diameter of 19 mm and a depth of 3 mm. The LCE ribbons, in their dispersed state, were heated from 25 to 175 °C to induce aggregation. Once aggregated and at a heated temperature of 175 °C, the aggregate was completely severed by using a pair of scissors (Westcott) to cut the aggregate into two separate pieces. After severing the aggregate, the two separate pieces were allowed to independently disperse, without stirring, by cooling the bath to 25 °C. Aggregate reformation was then initiated by heating the bath to 175 °C. The reformed structure was dispersed and reaggregated to understand the effect that aggregation and dispersion cycling has on aggregate reformation after damage. A digital camera was placed above the setup to record a video. The represented images are snapshots taken from the video. Supplementary Information provides additional information on aggregate reformation.

## Hydrogel ribbon injection

The injectability of hydrogel ribbons was investigated by first heating a bath of 1.5 ml of deionized water dyed with blue food colouring in a glass Petri dish to 37 °C. The temperature was monitored using a thermocouple (Traceable 4015CC). Once the water reached 37 °C, 40 mg of hydrogel ribbons, previously loaded into a syringe (BD 10 ml syringe) fixed with a 10 G needle tip (Rachel's Closeouts), was injected into the heated bath. A camera was positioned on top and on the side of the Petri dish to record hydrogel ribbon aggregation as a function of time.

## Cell culture

NIH 3T3 fibroblasts were cultured using HyClone Dulbecco's Modified Eagle Medium with high glucose (Cytiva) supplemented with 10% foetal bovine serum (Corning) and 1% penicillin–streptomycin (Life Technologies). Bilayer hydrogel samples were prepared using the aforementioned procedure with one difference. After spin coating the PMMA layer, the hydrogel solution was filled into the cell mould and polymerized for 1 min using a UV oven at an intensity of 2 mW cm$^{-2}$. The hydrogel layer of the bilayer sheet was functionalized before the cell studies using a secondary modification (2 mM arginylglycylaspartic

acid, 20 mg ml$^{-1}$ lithium phenyl-2,4,6-trimethylbenzoylphosphinate and 9 min of UV exposure). After initial polymerization, the glass slide from the hydrogel side of the mould was removed, and a new slide was placed 50 μm above the hydrogel. The integrin-binding motifs were filled above the hydrogel layer through capillary action and were allowed to swell into the hydrogel at 25 °C for 20 min before further polymerization in a UV oven at an intensity of 2 mW cm$^{-2}$ for 9 min. Bilayer hydrogels were then laser cut and placed under UV light of the biosafety cabinet (Labconco) for 30 min for sterilization. After sterilization, warm cell culture media were pipetted onto hydrogel ribbons, causing the ribbons to release. The ribbons were then transferred from the glass slide to 12-well plates. 3T3 fibroblasts (5M cells) were then seeded on the flat bilayer hydrogels at 25 °C and set for 30 min. After cell seeding, the ribbons were placed in an incubator (37 °C). The media were replaced every other day. After reaching confluence, 3T3 cells that were adhered to the hydrogel ribbons were stained with CellTracker Green CMFDA dye (Thermo Fisher Scientific) as per the manufacturer's protocol. Temperature-responsive ribbons with 3T3 fibroblasts were imaged using a Lionheart microscope (BioTek). The dispersion of cell-laden ribbons was imaged with temperature control (25/37 °C) to demonstrate self-assembling scaffolds. Cellular viability of the cell-laden ribbons was visualized using a calcein-AM-based live and dead assay (Invitrogen) at multiple time points (1, 3 and 7 days) after the initial cell seeding, following the manufacturer's protocol. The stained cell-laden ribbons were imaged using a Zeiss Axiovert A1 fluorescence microscope and Leica SP8 confocal microscope with appropriate filters. The metabolic activity of the cell-laden ribbons was evaluated at multiple time points (1, 2, 3, 5, 7 and 10 days) using alamarBlue assay (Thermo Fisher Scientific). For the alamarBlue assay, the ribbons were placed in Nunclon Sphera 96-well plates before seeding with 3T3 cells. These well plates prevent cell adhesion to the surface of the well, thereby allowing for an accurate assessment of the metabolic activity of cells adhered to the ribbons. Cell-laden ribbons were incubated with media containing 10% alamarBlue (v/v) for 2 h. The assay media were then collected and fresh media (without alamarBlue) were added back to the cells. The reduction of alamarBlue in the assay media was determined following the manufacturer's protocols by measuring the absorbance at 570 and 600 nm using a spectrophotometer (BioTek Cytation 5).

### Participants and procedures

Blood-clotting experiments were evaluated using human blood samples from healthy participants in compliance with the protocols that were approved by the institutional review board (IRB2022-0501D) at Texas A&M University. All participants gave informed consent before participation in the study.

### Data analysis

Statistical analysis for comparison of the yield stress of LCE ribbons with different offset angles was carried out by first testing for normality using the Shapiro–Wilk test using Origin. After normality was confirmed, a paired *t*-test was performed using Origin 9.9.

Statistical analysis for the blood-clotting experiments was carried out through an ordinary one-way analysis of variance with multiple comparisons using GraphPad Prism 9. The plots were created using IGOR Pro 7, GraphPad Prism 9 and MATLAB 2022a.

### Reporting summary

Further information on research design is available in the Nature Portfolio Reporting Summary linked to this article.

## Data availability

Data supporting the findings of this study are available in the Article and the Supplementary Information. Source data are provided with this paper.

## References

54. Dinkgreve, M., Paredes, J., Denn, M. M. & Bonn, D. On different ways of measuring 'the' yield stress. *J. Non-Newtonian Fluid Mech.* **238**, 233–241 (2016).

55. Perge, C., Taberlet, N., Gibaud, T. & Manneville, S. Time dependence in large amplitude oscillatory shear: a rheo-ultrasonic study of fatigue dynamics in a colloidal gel. *J. Rheol.* **58**, 1331–1357 (2014).

## Author contributions

M.K.A. and T.H.W. designed the research. M.K.A. conducted most of the experiments. R.J.W. and F.J.V. performed the simulations. M.S.K., M.Z. and C.M. performed and/or designed the experiments involving conductive ribbons. L.K.J. performed the experiments involving micro-computed tomography imaging. M.S.K., S.W., M.J. and A.D. assisted with the experiments involving mechanical testing. A.K.G., M.H.K. and K.A.S. performed and/or designed the experiments involving cell seeding. A.K.G. and S.E.H. performed and/or designed the experiments involving blood clotting. The Article was written through the contributions of all authors. All authors have given approval to the final version of the Article.

## Competing interests

The authors declare no competing interests.

## Additional information

**Extended data** is available for this paper at https://doi.org/10.1038/s41563-023-01761-4.

**Supplementary information** The online version contains supplementary material available at https://doi.org/10.1038/s41563-023-01761-4.

**Correspondence and requests for materials** should be addressed to Taylor H. Ware.

**Peer review information** *Nature Materials* thanks Christopher Yakacki and the other, anonymous, reviewer(s) for their contribution to the peer review of this work.

**Reprints and permissions information** is available at www.nature.com/reprints.
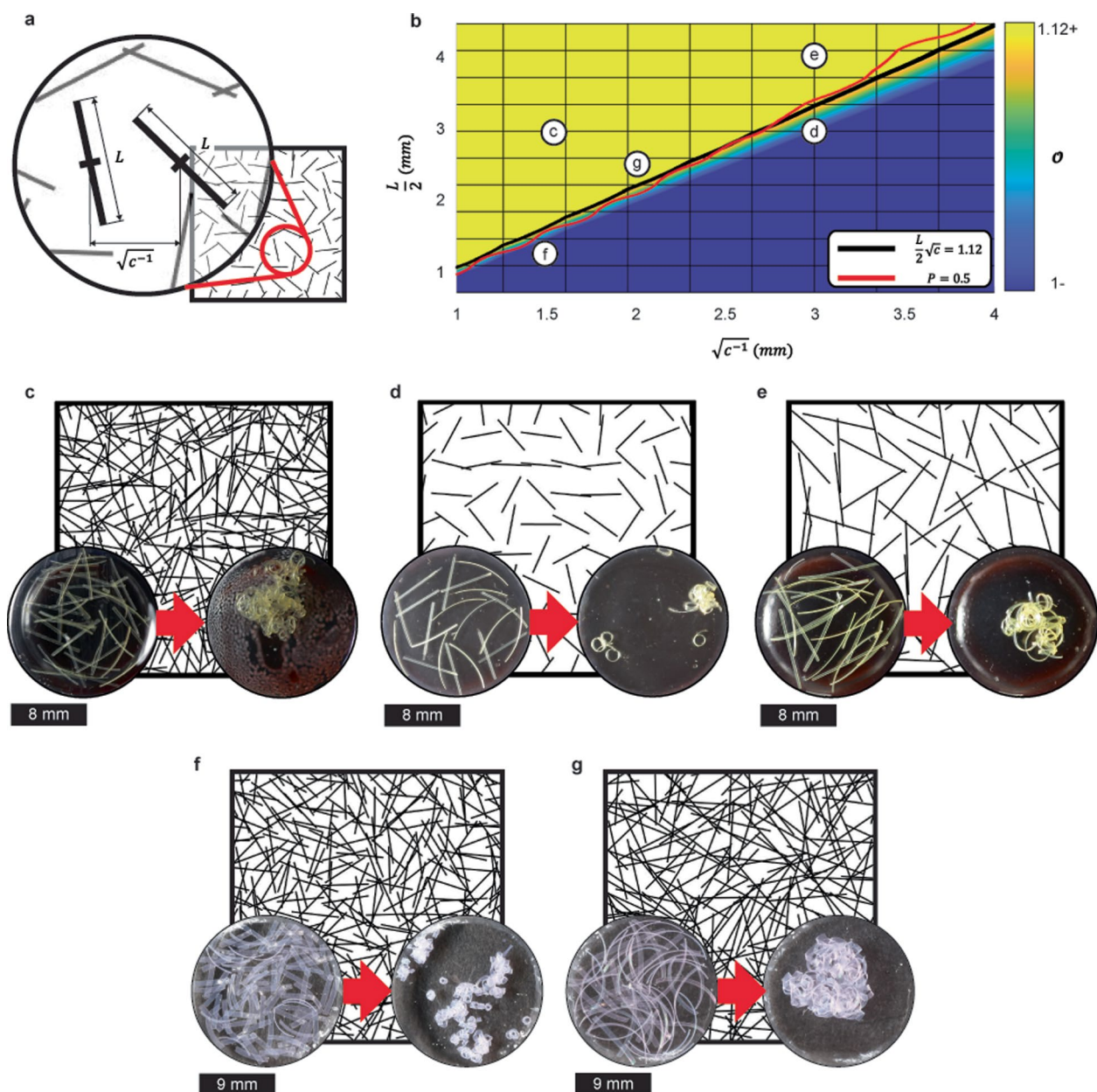
**Extended Data Fig. 1 | Overlap-dependent network aggregation. a**, A schematic of two ribbons with nominal separation $\sqrt{c^{-1}}$ and length $L$ defines the measures governing $\mathcal{O}$. **b**, Phase space of $\mathcal{O}$ for the range of ribbon separations, $\sqrt{c^{-1}}$, and reaches, $L/2$, investigated through the Monte Carlo model is presented. The heat map represents $\mathcal{O} \in [1, 1.12]$ such that the regime for which $\mathcal{O} > 1.12$ is depicted in yellow, while the regime for which $\mathcal{O} < 1$ (wherein percolation is impossible) is depicted in blue. The red line represents the phase boundary to the left of which percolation occurred at least 50% ($P \geq 0.5$) of the time when visually determined over $n = 10$ simulations for each parameter combination. **c-e**, Monte Carlo networks and snapshots of the real system

composed of LCE ribbons with an offset angle of 10° at 25 °C (left) and after heating to 175 °C (right) are shown for **c**, $L = 6$ mm, $\sqrt{c^{-1}} \approx 1.6$ mm ($\mathcal{O} > 1.12$); **d**, $L = 6$ mm, $\sqrt{c^{-1}} \approx 3$ mm ($\mathcal{O} < 1.12$); and **e**, $L = 8$ mm, $\sqrt{c^{-1}} \approx 3$ mm ($\mathcal{O} > 1.12$). **f,e**, Monte Carlo networks and snapshots of the real system composed of bilayer hydrogel ribbons at 25 °C (left) and after heating to 37 °C (right) are shown for **f**, $L = 5$ mm, $\sqrt{c^{-1}} \approx 1.5$ mm ($\mathcal{O} < 1.12$); and **g**, $L = 10$ mm, $\sqrt{c^{-1}} \approx 2$ mm ($\mathcal{O} > 1.12$). Unlike the reach of LCE ribbons, the reach of hydrogel ribbons decreases by approximately 50% as a function of temperature due to deswelling (Supplementary Fig. 5).
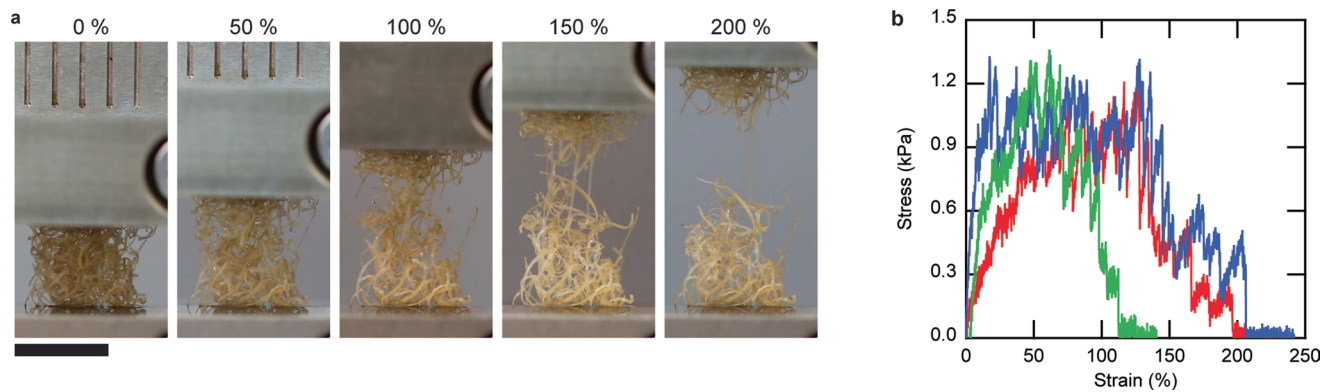
**Extended Data Fig. 2 | Semicrystalline LCE aggregates can withstand tensile loads. a**, Timelapse photographs of tensile test of a representative sample of an aggregate created from semicrystalline LCEs at strains of 0%, 50%, 100%, 150%, and 200% (Scale bar = 6 mm). **b**, Stress plotted as a function of strain of semicrystalline aggregates. Tests were performed 3 times, using 3 separate samples of aggregated semicrystalline LCEs. All plots are shown.

# nature portfolio

| Corresponding author(s): | Taylor Ware |
|---|---|
| Last updated by author(s): | Nov 7, 2023 |

# Reporting Summary

Nature Portfolio wishes to improve the reproducibility of the work that we publish. This form provides structure for consistency and transparency in reporting. For further information on Nature Portfolio policies, see our Editorial Policies and the Editorial Policy Checklist.

## Statistics

For all statistical analyses, confirm that the following items are present in the figure legend, table legend, main text, or Methods section.

| n/a | Confirmed | |
|---|---|---|
| ☐ | ☒ | The exact sample size (*n*) for each experimental group/condition, given as a discrete number and unit of measurement |
| ☐ | ☒ | A statement on whether measurements were taken from distinct samples or whether the same sample was measured repeatedly |
| ☐ | ☒ | The statistical test(s) used AND whether they are one- or two-sided<br>*Only common tests should be described solely by name; describe more complex techniques in the Methods section.* |
| ☒ | ☐ | A description of all covariates tested |
| ☐ | ☒ | A description of any assumptions or corrections, such as tests of normality and adjustment for multiple comparisons |
| ☐ | ☒ | A full description of the statistical parameters including central tendency (e.g. means) or other basic estimates (e.g. regression coefficient) AND variation (e.g. standard deviation) or associated estimates of uncertainty (e.g. confidence intervals) |
| ☐ | ☒ | For null hypothesis testing, the test statistic (e.g. *F*, *t*, *r*) with confidence intervals, effect sizes, degrees of freedom and *P* value noted<br>*Give P values as exact values whenever suitable.* |
| ☒ | ☐ | For Bayesian analysis, information on the choice of priors and Markov chain Monte Carlo settings |
| ☒ | ☐ | For hierarchical and complex designs, identification of the appropriate level for tests and full reporting of outcomes |
| ☒ | ☐ | Estimates of effect sizes (e.g. Cohen's *d*, Pearson's *r*), indicating how they were calculated |

*Our web collection on statistics for biologists contains articles on many of the points above.*

## Software and code

Policy information about availability of computer code

| Data collection | Computational simulation was performed by using MATLAB R2022a. |
|---|---|
| Data analysis | Image analysis was performed by using ImageJ 1.53e. Statistical analysis was performed using Origin 9.9 and Prism 9. MATLAB R2022a was also used for data analysis. BioTek Gen5 was used to analyze absorbance of alamarBlue. RheoCompass 1.3 and Trios 5.2 software was used to collect mechanical testing data. Igor Pro 7 was used for plotting data. |

For manuscripts utilizing custom algorithms or software that are central to the research but not yet described in published literature, software must be made available to editors and reviewers. We strongly encourage code deposition in a community repository (e.g. GitHub). See the Nature Portfolio guidelines for submitting code & software for further information.

## Data

Policy information about availability of data

All manuscripts must include a data availability statement. This statement should provide the following information, where applicable:
- Accession codes, unique identifiers, or web links for publicly available datasets
- A description of any restrictions on data availability
- For clinical datasets or third party data, please ensure that the statement adheres to our policy

Data supporting the findings of this study are available in the article and its supplementary files. Source data are provided with this manuscript.

## Research involving human participants, their data, or biological material

Policy information about studies with <u>human participants or human data</u>. See also policy information about <u>sex, gender (identity/presentation), and sexual orientation</u> and <u>race, ethnicity and racism</u>.

| | |
|---|---|
| Reporting on sex and gender | Sex- and gender-based analysis was not conducted because the studies involving human blood were intended as studies to evaluate the potential of aggregates formed from hydrogel ribbons to clot whole blood. Only one biological replicate was performed for each study (clotting time test; aneurysm clotting model), so it is not possible to draw conclusions based on sex or gender. Material replicates are present to allow for evaluation of non-biological influences (i.e., temperature, material homogeneity, etc.). Sex was self-reported during participant screening, but was not taken into consideration for the study. Informed consent was obtained for sharing de-identified data. |
| Reporting on race, ethnicity, or other socially relevant groupings | There were no socially constructed or socially relevant categorization variables used in the study. Human blood was used to evaluate clotting on a macro-level, with regard only to the overall clotting time. No individual identifiers were evaluated with respect to the acquired blood. |
| Population characteristics | See above; no covariate-relevant population characteristics of the human research participants were evaluated for this pilot study. |
| Recruitment | Participants were recruited through advertisements posted in the Texas A&M University Student Health Center. A possible self-selection bias is present in that participants were likely to be college-aged (i.e., young). This is unlikely to have impacted results because donors were screened for medical history related to clotting and excluded from the study if they did have any preexisting clotting conditions or took medications that may have impacted clotting. |
| Ethics oversight | Texas A&M University Institutional Review Board number IRB2022-0501D |

Note that full information on the approval of the study protocol must also be provided in the manuscript.

# Field-specific reporting

Please select the one below that is the best fit for your research. If you are not sure, read the appropriate sections before making your selection.

☒ Life sciences  ☐ Behavioural & social sciences  ☐ Ecological, evolutionary & environmental sciences

For a reference copy of the document with all sections, see <u>nature.com/documents/nr-reporting-summary-flat.pdf</u>

# Life sciences study design

All studies must disclose on these points even when the disclosure is negative.

| | |
|---|---|
| Sample size | No statistical methods were used to predetermine the sample size. The appropriate sample size was determined based on the previously published literature (Gaharwar, A.K., Adv. Mat. Int., 10, 2022) on polymer biocompatibilty. The sample size for polymer biocompatibilty was n = 4. |
| Data exclusions | No data was excluded from the analysis. |
| Replication | Cell viability and cell proliferation were measured from at least 3 independent material replications yielding similar results. |
| Randomization | Randomization was not relevant to our experiments as all hydrogel ribbons were fabricated in a similar manner and all cells were seeded on hydrogel ribbons in a similar manner. There is no variation in the synthesis or cell seeding treatment between samples. |
| Blinding | Blinding was not relevant to our study as the absorbance was measured using a spectrophotometer (BioTek Cytation 5), enabling unbiased quantification of cell viability and cell proliferation. |

# Reporting for specific materials, systems and methods

We require information from authors about some types of materials, experimental systems and methods used in many studies. Here, indicate whether each material, system or method listed is relevant to your study. If you are not sure if a list item applies to your research, read the appropriate section before selecting a response.

## Materials & experimental systems

| n/a | Involved in the study |
|-----|----------------------|
| ☒ | ☐ Antibodies |
| ☐ | ☒ Eukaryotic cell lines |
| ☒ | ☐ Palaeontology and archaeology |
| ☐ | ☒ Animals and other organisms |
| ☒ | ☐ Clinical data |
| ☒ | ☐ Dual use research of concern |
| ☒ | ☐ Plants |

## Methods

| n/a | Involved in the study |
|-----|----------------------|
| ☒ | ☐ ChIP-seq |
| ☒ | ☐ Flow cytometry |
| ☒ | ☐ MRI-based neuroimaging |

# Eukaryotic cell lines

Policy information about cell lines and Sex and Gender in Research

| | |
|---|---|
| Cell line source(s) | NIH 3T3 mouse fibroblasts (CRL-1658, ATCC). |
| Authentication | NIH 3T3 fibroblasts were authenticated by ATCC and not the authors. Cells passed all testing protocols. Cell count and post-freeze viability were conducted using Trypan Blue Stain method. Growth properties and morphology were observed visually. Mycoplasma contamination was tested using a Hoechst DNA staining method, agar culture method, and a PCR-based assay. Species determination was conducted using a COI assay. Sterility test (BacT/ALERT 3D) was performed using a iAST bottle (aerobic) at 32.5 °C and a iNST bottle (anaerobic) at 32.5 °C. Contact inhibition test was also performed. |
| Mycoplasma contamination | All cell lines used tested negative for mycoplasma contamination prior to use with a mycoplasma detection assay (Lonza). |
| Commonly misidentified lines (See ICLAC register) | No commonly misidentified cell lines were used. |

# Animals and other research organisms

Policy information about studies involving animals; ARRIVE guidelines recommended for reporting animal research, and Sex and Gender in Research

| | |
|---|---|
| Laboratory animals | The study did not involve laboratory animals. |
| Wild animals | Fire ant (S. Invicta) workers (all sterile female specimen) were captured and photographed for this manuscript. No quantitative analysis was conducted or reported on ants in the scope of this work. Worker ants were caught by identifying fire ant mounds, breaching their top surfaces with a smoothly rounded trowel, placing the trowel on top of the breach, and then manually perturbing it so that swarming worker ants fell into its base. The ants were then transported to an empty container until on the order of several thousand workers had been isolated from debris. The container was then inspected to ensure that no eggs, larvae, or pupae (i.e., reproducing members of the colony) entered the population. Commercially bought potting soil was then added to the container, along with test tubes of water and food, prior to transportation and storage. Ants from several colonies were collected, however each colony was stored in a separate container. Ant populations were kept alive in their containers with regular supply of food and water until they naturally died after several weeks. |
| Reporting on sex | All fire ant (S. Invicta) workers are female. No quantitative analysis was conducted or reported on ants in the scope of this work. |
| Field-collected samples | Populations of fire ants (S. Invicta) were kept in lidded, plastic containers with a layer of potting soil at their bottoms for nesting. The containers were stored at room temperature (approximately 21˚C). Food and fresh water were provided, and waste (e.g., dead ants, food waste, etc.) was removed daily. After 6-8 weeks, once a population had naturally expired, the soil was gently stirred with forceps to ensure that no living ants remained. The soil was then sterilized for 24 hours with a mixture of water and isopropyl alcohol before disposal. No quantitative analysis was conducted or reported on ants in the scope of this work. |
| Ethics oversight | No ethical approval or guidance was required as no vertebrates or higher invertebrates were studied in the scope of this work. |

Note that full information on the approval of the study protocol must also be provided in the manuscript.